Bearingless Twin Drive as Axial-Flow Pump Application

Wolfgang GRUBER*, Patrick ZORN*, Edmund MARTH* and Christopher WALL**
* Institute of Electric Drives and Power Electronics, Johannes Kepler University Linz
Altenberger Str. 69, 4040 Linz, Austria
E-mail: wolfgang.gruber@jku.at
** Cardiology Devices Ltd
2 Pavilion Court, 600 Pavilion Drive, Northampton NN4 7SL, United Kingdom

Abstract
This paper presents the concept, design, and prototyping of a novel axial-flow pump system based on a bearingless twin drive configuration. Bearingless motors eliminate the need for mechanical bearings by utilizing magnetic forces for rotor suspension and torque generation, making them highly suitable for compact, high-reliability applications. The proposed system employs two bearingless motors on a shared hollow-shaft rotor to achieve five degrees of freedom actively controlled, with the axial direction passively stabilized by magnetic reluctance forces. The system targets low-power applications, operating at 5,000-10,000 rpm with a torque of 15-40 mNm and constrained to a compact geometry with an outer diameter below 50 mm.
The study investigates optimal winding topologies and motor configurations using analytical and numerical methods. A comprehensive analysis of five- and six-phase systems with varying stator slot/rotor pole combinations was performed to evaluate torque and suspension force capability, considering non-overlapping concentric winding schemes to minimize axial length. Geometry optimization was carried out using finite element simulations, focusing on maximizing torque and suspension force while reducing losses and destabilizing forces.
Ultimately, a six-phase, twelve-slot stator design with seven rotor pole pairs was chosen due to its superior electromagnetic performance and manufacturability. A prototype was built and is currently undergoing testing. This work demonstrates the feasibility of miniaturized axial-flow pumps using bearingless twin drives, offering significant potential in medical and precision engineering applications where compactness, efficiency, and minimal maintenance are critical.

Keywords : Bearingless Motor, Axial-Flow Pump, Topology Selection, Geometry Optimization

1. Introduction

Magnetically levitated pumps are designed without traditional mechanical bearings, which are typically used to support rotating components. Instead, magnetic forces are employed to suspend the rotor. Bearingless systems combine force and torque generation within a single unit, resulting in a highly compact design. This approach eliminates friction, reduces wear, and enhances efficiency by minimizing energy losses. Bearingless pumps are particularly advantageous in applications requiring high reliability, low maintenance, high purity, and long service life—such as in high-speed, high-pressure, or harsh environments. Their ability to operate without direct contact between moving parts also contributes to quieter and more efficient performance. The bearingless slice motor concept [1], in particular, has been successfully applied in pumps used in the medical [2] and semiconductor industries [3].

This manuscript introduces a novel axial-flow pump concept based on a pair of bearingless motors mounted on a common shaft, referred to as a bearingless twin drive. This configuration, illustrated in Fig. 1, is typically used in high-power, high-speed systems [4]–[7] to minimize shaft length. In our work, we adopt this architecture to exploit its compactness, but focus on significantly lower power levels.

In the proposed design, two bearingless motors—each generating radial forces—actively stabilize a permanent-magnet hollow-shaft rotor in five degrees of freedom, including rotation. The sixth degree of freedom, axial motion, is passively stabilized by permanent magnetic reluctance forces. Pumping action is achieved through blades mounted inside the hollow rotor shaft.

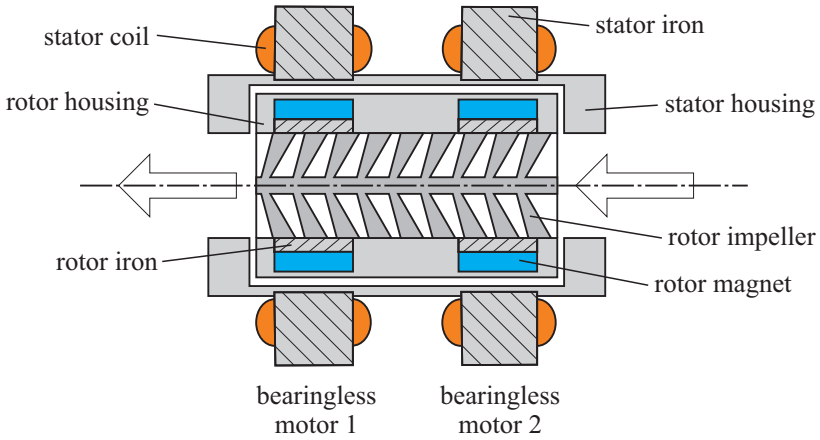

Fig. 1: Basic setup of the bearingless twin drive axial-flow pump system.

2. Bearingless Motor Design

The target system is designed to operate at 5,000-10,000 rpm and deliver a torque of 15-40 mNm. Strict constraints are imposed on both the radial and axial dimensions; ideally, the overall length and diameter should not exceed 5 cm. Prior to geometry optimization, suitable bearingless motor topologies are analyzed analytically—specifically with respect to stator slot and rotor pole-pair combinations—while considering both suspension force and torque performance. To minimize the axial winding head and thus reduce the overall axial length of the system, only concentric windings with a single winding step (i.e., without overlapping) are considered. A multiphase combined winding system, as proposed in [8], is adopted to ensure high efficiency and compact design. Both single-layer and double-layer winding configurations, as well as slotted and slotless stator topologies, are evaluated. Furthermore, the analysis is restricted to five- and six-phase motor designs in order to limit the number of required half-bridges in the power electronics, thereby simplifying the system and reducing cost.

2.1. Torque and Force Winding Factors

For interior rotor surface-mounted permanent magnet bearingless motors, the single-phase force components (F_x and F_y) and torque (T_z) of the first phase can be expressed as [9]

$$\begin{pmatrix} F_{x,1}(\varphi_r) \\ F_{y,1}(\varphi_r) \\ T_{z,1}(\varphi_r) \end{pmatrix} = \begin{pmatrix} -\hat{F}_x \cos(p_r\varphi_r) \\ \hat{F}_y \sin(p_r\varphi_r) \\ \hat{T}_z \sin(p_r\varphi_r) \end{pmatrix} i_1, \tag{1}$$

where φ_r is the mechanical rotor angle, and p_r denotes the number of rotor pole pairs. The amplitude values $\hat{F}_x$, $\hat{F}_y$, and $\hat{T}z$ depend on factors such as the motor geometry, materials used, and the chosen winding scheme. In this work, we focus on the influence of the winding scheme. The winding factor quantifies how effectively a specific winding configuration can generate an air-gap field of a given harmonic order. The conventional torque-generating winding factor is calculated for the harmonic order produced by the rotor magnets, i.e., for $p_s = p_r$, and is denoted as $\xi_t = \xi_{p_r}$. It is also well known that radial suspension forces arise when the winding scheme can generate harmonic components corresponding to $p_s = p_r \pm 1$. This leads us to define a winding factor for suspension force, ξ_f, as the maximum of ξ_{p_r+1} and ξ_{p_r-1}.

For a given winding configuration, the generated suspension forces and drive torque are proportional to their respective winding factors ξ_f and ξ_t. Therefore, the rated suspension forces and torque of the first phase can be rewritten as

$$\begin{pmatrix} F_{x,1}(\varphi_r) \\ F_{y,1}(\varphi_r) \\ T_{z,1}(\varphi_r) \end{pmatrix}_r = \begin{pmatrix} -\xi_f \cos(p_r\varphi_r) \\ e\xi_f \sin(p_r\varphi_r) \\ \xi_t \sin(p_r\varphi_r) \end{pmatrix} i_1, \tag{2}$$

where e is a factor between 0 and 1 indicating the ellipticity of the single-phase suspension force characteristic [9], [10]. In this study, we assume $e = 1$, resulting in a fully circular suspension force orbit.

2.2. Torque and Force Performance Factors

Based on the single-phase characteristics of the first phase, the behavior of the remaining $m-1$ phases can be determined using

$$\begin{pmatrix} F_{x,n}(\varphi_r) \\ F_{y,n}(\varphi_r) \\ T_{z,n}(\varphi_r) \end{pmatrix}_r = \begin{pmatrix} \cos(\tau(n-1)) & -\sin(\tau(n-1)) & 0 \\ \sin(\tau(n-1)) & \cos(\tau(n-1)) & 0 \\ 0 & 0 & 1 \end{pmatrix} \begin{pmatrix} F_{x,1}(\varphi_r - \tau p_r(n-1)) \\ F_{y,1}(\varphi_r - \tau p_r(n-1)) \\ T_{z,1}(\varphi_r - \tau p_r(n-1)) \end{pmatrix}_r i_n, \tag{3}$$

where $\tau = 2\pi/m$ and n denotes the phase index. The complete force-current relationship is described by the rated force-current matrix $\mathbf{T}_{\mathbf{m}r}(\varphi_r)$, obtained by assembling all phase contributions

$$\begin{pmatrix} F_x(\varphi_r) \\ F_y(\varphi_r) \\ T_z(\varphi_r) \end{pmatrix}_r = \left(\begin{pmatrix} F_{x,1}(\varphi_r) \\ F_{y,1}(\varphi_r) \\ T_{z,1}(\varphi_r) \end{pmatrix}_r \begin{pmatrix} F_{x,2}(\varphi_r) \\ F_{y,2}(\varphi_r) \\ T_{z,2}(\varphi_r) \end{pmatrix}_r \cdots \begin{pmatrix} F_{x,m}(\varphi_r) \\ F_{y,m}(\varphi_r) \\ T_{z,m}(\varphi_r) \end{pmatrix}_r \right) \mathbf{i_s} = \mathbf{T}_{\mathbf{m}r}(\varphi_r)\mathbf{i_s}, \tag{4}$$

where the phase current vector is defined as $\mathbf{i_s} = (i_1 \;\; i_2 \;\; \cdots \;\; i_m)^T$. This matrix, which characterizes the overall motor behavior, is directly determined by the selected winding scheme, specifically through the winding factors ξ_f and ξ_t, and depends on the number of pole pairs p_r and phases m.

To determine the required phase currents for a desired force and torque output, the inverse relation is used, involving the rated current-force matrix $\mathbf{K}_{\mathbf{m}r}(\varphi_r)$, which satisfies $\mathbf{T}_{\mathbf{m}r}(\varphi_r)\mathbf{K}_{\mathbf{m}r}(\varphi_r) = \mathbf{I}_3$, where $\mathbf{I}_3$ s the 3×3 identity matrix. This inverse is computed under the constraints of a star-connected system $i_1 + i_2 + \cdots + i_m = 0$ and optimized for efficiency by minimizing $\mathbf{i_s}\mathbf{i_s}^T$, resulting in

$$\mathbf{K}_{\mathbf{m}r}(\varphi_r) = \left(\mathbf{T}_{\mathbf{m}r}(\varphi_r)^T - \frac{1}{m}\mathbf{J}_m\mathbf{T}_{\mathbf{m}r}(\varphi_r)^T\right)\left(\mathbf{T}_{\mathbf{m}r}(\varphi_r)\left(\mathbf{T}_{\mathbf{m}r}(\varphi_r)^T - \frac{1}{m}\mathbf{J}_m\mathbf{T}_{\mathbf{m}r}(\varphi_r)^T\right)\right)^{-1}, \tag{5}$$

where $\mathbf{J}_m$ denotes the $m \times m$ all-ones matrix. The matrix $\mathbf{K}_{\mathbf{m}r}(\varphi_r)$ enables evaluation of motor performance. Smaller matrix entries are preferred, as they indicate that lower phase currents are needed to generate a given force or torque. This motivates the definition of performance factors for both torque and suspension force generation. Silber [11] originally proposed a torque performance factor, which we redefine here (using the maximum instead of root mean square values and scaling by $2/m$ as

$$k_t = \frac{2}{\sum_{i=1}^{m} \max\left(\mathbf{K}_{\mathbf{m}r_{(i,3)}}(\varphi_r)\right)} \tag{6}$$

and similarly, the suspension force performance factor is defined as

$$k_f = \frac{4}{\sum_{i=1}^{m}\sum_{j=1}^{2} \max\left(\mathbf{K}_{\mathbf{m}r_{(i,j)}}(\varphi_r)\right)}, \tag{7}$$

where $\mathbf{K}_{\mathbf{m}r(i,j)}(\varphi_r)$ represents the element in row j and column i of the matrix. Higher values of k_t and k_f indicate more efficient generation of torque and suspension force with lower current, and are therefore considered advantageous.

In summary, the four factors—ξ_t, ξ_f, k_t, and k_f—can be used to assess the suitability of a winding scheme for bearingless motor operation. High values for all these factors are essential for achieving good performance in bearingless motor topologies.

3. Topology Selection

In this application, both the overall size and axial length are highly constrained, with the winding head of the coils representing a particularly significant contribution to the system's length. To address this, distributed windings—where winding heads overlap—are avoided. Instead, only concentric coils are considered, either wound directly around the stator teeth or implemented as air-gap coils.

For the same reason, double-layer winding systems are preferred, as they help minimize the axial extent of the winding head. The number of phases m is restricted to five or six to limit complexity and component count. Furthermore, the total number of individual coils is kept below 20, as a higher coil count results in smaller coil sizes, which are increasingly difficult to manufacture.

3.1. Five-Phase Winding Systems

In this section, we consider stator configurations with five, ten, and fifteen slots. For each slot number, we examine feasible winding schemes and corresponding rotor pole pair counts. To assess the behavior of the bearingless motor, we analyze the associated winding designs and performance metrics. Table 1 presents the results for the five-slot configuration. In this case, only a double-layer winding scheme, as illustrated in Fig. 2, is feasible. The optimal choice for this winding is a rotor equipped with either three or eight permanent magnet pole pairs.

Table 1: Winding and performance factors of the bearingless motors with five stator phases and slots.

p_r	ξ_t	ξ_f	k_t	k_f
1+5n	0.588	0.951	0.588	0.951
2+5n	0.951	0.951	0	0
3+5n	0.951	0.951	0.951	0.951
4+5n	0.588	0.951	0	0
5+5n	0	0.588	0	0

Note: n in rotor pole number stands for a non-negative integer.

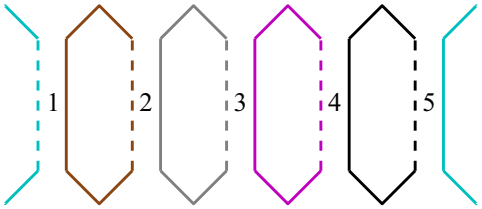

Fig. 2: Referring five-slot double-layer winding system.

Additionally, we present the results for a system with fifteen stator slots. In this case, the double-layer winding shown in Fig. 3 is examined. The performance factors are summarized in Table 2. From these results, it is evident that the five-phase bearingless motor with sixteen rotor poles represents a very promising design.

Table 2: Winding and performance factors of the bearingless motors with five stator phases and fifteen slots.

p_r	ξ_t	ξ_f	k_t	k_f
4	0.3	0.577	0	0
5	0.577	0.83	0	0
6	0.83	0.98	0.83	0.98
7	0.98	0.98	0	0
8	0.98	0.98	0.98	0.98
9	0.83	0.98	0	0
10	0.577	0.83	0	0
11	0.3	0.577	0.3	0.577

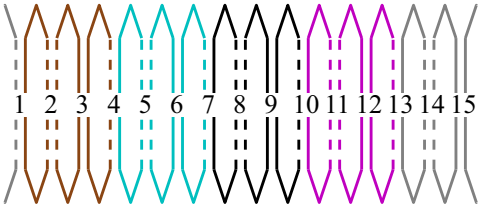

Fig. 3: Referring fifteen-slot double-layer winding system.

The performance and winding factors of all five-phase winding schemes featuring non-overlapping concentric coils within the design space are evaluated. It was found that such bearingless motors can be implemented with rotor pole pairs $p_r = 1, 3, 6, 8, 11$, and 13. However, considering the performance factor, the fifteen-slot configuration with eight rotor poles appears to be the most promising.

3.2. Six-Phase Winding Systems

Similar to the five-phase system, we analyze six-phase systems by taking a closer look at the winding and performance factors. In the following, three such winding designs are presented, featuring six, twelve, and eighteen stator slots. Notably, a rotor pole pair number of seven yields the best results for both the twelve- and eighteen-slot stator configurations.

Table 3: Winding and performance factors of the bearingless motors with six stator phases and slots.

p_r	ξ_t	ξ_f	k_t	k_f
1+6n	0.5	0.866	0.5	0.866
2+6n	0.866	1	0	0
3+6n	1	0.866	0	0.782
4+6n	0.866	1	0.866	1
5+6n	0.5	0.866	0	0
6+6n	0	0.5	0	0.1

Note: n in rotor pole number stands for a non-negative integer.

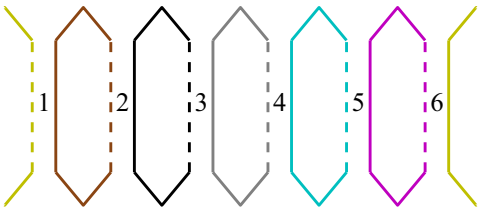

Fig. 4: Referring six-slot double-layer winding system.

Table 4: Winding and performance factors of the bearingless motors with six stator phases and twelve slots.

p_r	ξ_t	ξ_f	k_t	k_f
4	0.75	0.933	0.75	0.933
5	0.933	1	0	0
6	1	0.933	0	0.11
7	0.933	1	0.933	1
8	0.75	0.933	0	0
9	0.5	0.75	0	0.61
10	0.25	0.5	0.25	0.5

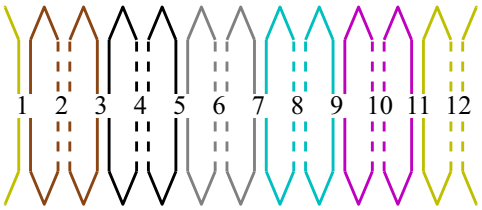

Fig. 5: Referring twelve-slot double-layer winding system.

Table 5: Winding and performance factors of the bearingless motors with six stator phases and eighteen slots.

p_r	ξ_t	ξ_f	k_t	k_f
6	0.577	0.902	0	0.2
7	0.902	0.725	0.902	0.725
8	0.725	0.902	0	0
9	0.333	0.725	0	0.59
10	0.725	0.902	0.725	0.902
11	0.902	0.725	0	0
12	0.577	0.902	0	0.2

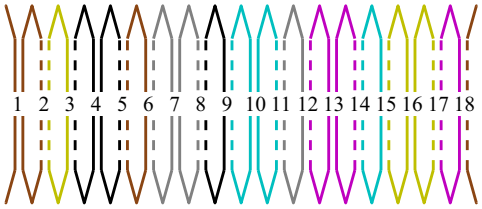

Fig. 6: Referring eighteen-slot double-layer winding system.

Generally, for six-phase windings, only rotors producing pole pair numbers of one, seven, ten, and thirteen result in feasible bearingless motors. To identify which of these promising design variants performs best, a full geometry optimization is conducted. Both slotless stators (with concentric air gap coils) and slotted stators (with tooth coils) are considered in this process.

4. Optimization

The geometry of several promising bearingless motors is optimized in our simulation environment SyMspace [12] using two-dimensional finite element simulations in FEMM [13]. The optimization aims to maximize drive torque and suspension forces while minimizing losses, radial stiffness, and overall axial system length. A high torque factor combined with a low axial length is clearly most desirable.

The outer diameter of the stator, the inner diameter of the hollow-shaft rotor, and the air gap are kept constant.

Figure 7 presents two simulation results comparing different topologies. The destabilizing radial stiffness k_{bx} is plotted against the suspension force factor k_{bi}, where a high k_{bi} and low k_{bx} are preferred. Additionally, the torque factor k_{ti} is shown as a function of the axial motor length l_s.

From these results, it is evident that the slotted five-phase system exhibits the most promising characteristics, followed by the slotted six-phase system.

Obviously, we decided to investigate the five-phase system in more detail using three-dimensional finite element simulations. Unfortunately, it became apparent that due to the unsymmetrical stator design, significant permanent magnetic reluctance forces occur. These forces can be reduced by adding pole shoes to the stator slots. However, this approach complicates the manufacturing process, as it prevents the simple external fabrication of stator coils that can later be easily slipped onto the stator teeth.

The six-phase system does not suffer from this drawback, and cogging torque remains low even without stator pole shoes. Therefore, it was decided to build the first prototype based on the six-phase design. Another advantage of the six-phase winding system in twin bearingless drives is its potential to be configured as a dual-purpose no-voltage (DPNV) winding system, which could allow the reduction of three out of twelve half-bridges [4].

5. Prototype

After optimization, all geometric parameters, of whose some are summarized in Table 6, were finalized. Figure 8 shows the optimized cross-section to scale. The electromagnetic characteristic data obtained from the three-dimensional

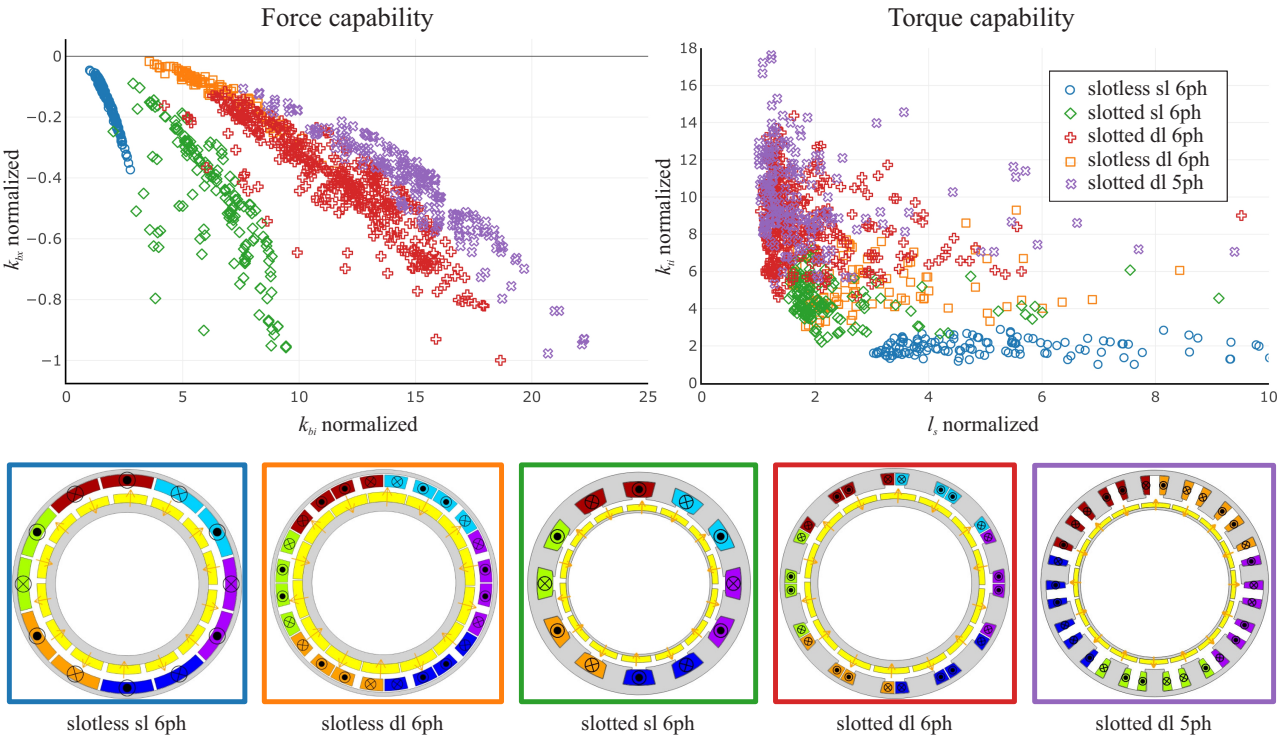

Fig. 7: Simulation results for different bearingless motor topologies (sl stands for single-layer and dl for double-layer winding scheme, while 6ph denotes a six-phase and 5ph a five-phase bearingless motor).

finite element simulations are presented in Table 7. It turned out that, due to the large air gap and the small height of the permanent magnets, two- and three-dimensional simulations show significant differences, as end effects are pronounced.

Table 6: Optimized geometry of the prototype bearingless motor with $N_s = 12$ and $p_r = 7$.

Variable	Description	Value	Unit
d_{so}	stator outer diameter	50	mm
d_{si}	stator inner diameter	33	mm
l_{sfe}	stator iron axial length	10	mm
l_s	stator overall axial length	16.8	mm
N_c	coil turn number	30	
δ	air gap length	1	mm
d_{ri}	rotor inner diameter	28	mm
b_m	magnet width	6	mm

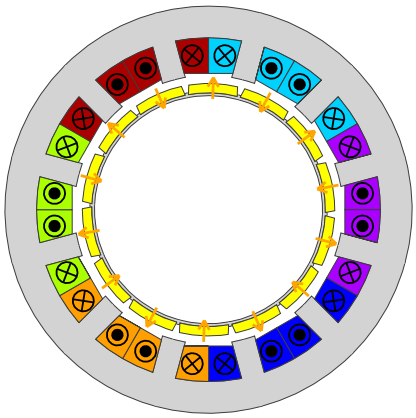

Fig. 8: Cross section of optimized bearingless motor.

Table 7: Electromagnetic characteristic of the optimized prototype bearingless motor.

Variable	Description	Value	Unit
R_s	stator phase resistance	220	mΩ
L_s	stator phase inductance	65	µH
I_s	rated stator terminal rms current	710	mA
U_s	rated stator rms phase voltage	4	V
k_{ti}	torque constant	21	mNm/A
k_{fi}	force constant	1	N/A
k_{bx}	radial stiffness	-17	N/mm
k_z	axial stiffness	0.9	N/mm
η	rated motor efficiency	93	%

Finally, the complete system—including eddy current sensors for position detection and Hall sensors for rotor angle measurement—is designed for manufacture. The left image in Fig. 9 shows a cross-section of the final design, featuring a thin titanium rotor housing. The outer stator housing is also made of titanium, while the inner stator uses epoxy resin to provide a tight seal against the pumped fluid. The cross-section includes the main dimensions.

The original space constraints are nearly met. However, it should be noted that the power electronics and sensor evaluation board are not integrated inside the pump but operate externally.

The photo on the left in Fig. 9 shows the stator at its actual size. The coils and lamination stack are original components, while the housing is a rapid prototyping mock-up.

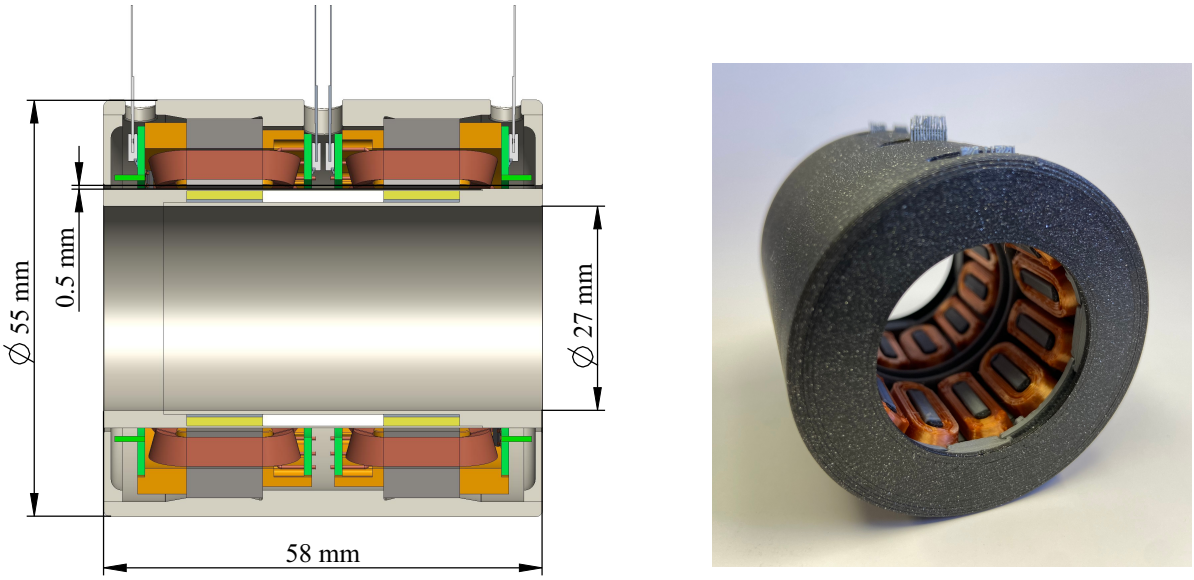

Fig. 9: Computer-aided design cross-section and photo of the prototype stator.

6. Conclusion and Outlook

This work analyzed small-power bearingless five- and six-phase systems featuring non-overlapping winding heads to minimize axial dimensions. By employing a twin bearingless drive configuration, five degrees of freedom are actively controlled, while only the axial direction remains passively stabilized by reluctance forces. The feasibility of building a very compact axial-flow pump with this design was demonstrated through finite element simulations.

Currently, the system is under manufacture, with parts of the stator and rotor already completed. In the near future, initial measurements will be conducted to verify the passive stiffness values as well as the motor's active force and torque capabilities. This will be followed by commissioning of the sensors and the bearingless motor. Finally, pump tests are planned to complete the evaluation.

Acknowledgments

This work was conducted within the COMET K2 Center for Symbiotic Mechatronics at the Linz Center of Mechatronics (LCM), funded by the Austrian and Upper Austrian governments. The authors gratefully acknowledge their support.

References

[1] R. Schöb and N. Barletta, "Principle and application of a bearingless slice motor," in *Proceedings of the 5th International Symposium on Magnetic Bearings*, 1996, pp. 313–318.

[2] N. Barletta and R. Schöb, "Design of a bearingless blood pump," in *Proceedings of the 3rd International Symposium on Magnetic Suspension Technology*, 1995, pp. 365–274.

[3] M. Neff, N. Barletta, and R. Schöb, "Bearingless centrifugal pump for highly pure chemicals," in *Proceedings of the 8th International Symposium on Magnetic Bearings*, 2002, pp. 283–288.

[4] Z. Wang and E. Severson, "Twin bearingless machine drive configurations with a reduced number of inverters," *IEEE Transactions on Energy Conversion*, vol. 38, no. 2, pp. 1130–1142, 2023.

[5] Y. Fu, M. Takemoto, S. Ogasawara, and K. Orikawa, "Investigation of a high speed and high power density bearingless motor with neodymium bonded magnet," in *Proceedings of the IEEE International Electric Machines and Drives Conference*, 2017.

[6] M. Ohsawa, "Study of the induction type bearingless motor," in *Proceedings of the 7th International Symposium on Magnetic Bearings*, 2000, pp. 389–394.

[7] R. Jastrzebski, P. Jaatinen, A. Chiba, and O. Pyrhonen, "Efficiency of buried permanent magnet type 5 kw and 50 kw high-speed bearingless motors with 4-pole motor windings and 2-pole suspension windings," in *Proceedings of the 15th International Symposium on Magnetic Bearings*, 2016.

[8] A. Khamitov, W. Gruber, G. Bramerdorfer, and E. Severson, "Comparison of combined winding strategies for radial nonsalient bearingless machines," *IEEE Transactions on Industry Applications*, vol. 57, no. 6, pp. 6856–6869, 2021.

[9] W. Gruber, S. Silber, W. Amrhein, and T. Nussbaumer, "Design variants of the bearingless segment motor," in *Proceedings of the International Symposium on Power Electronics, Electrical Drives, Automation and Motion*, 2010, pp. 1448–1453.

[10] K. Nenninger, W. Amrhein, and S. Silber, "Bearingless single-phase motor with fractional pitch windings," in *Proceedings of the 7th International Symposium on Magnetic Bearings*, 2000, pp. 371–376.

[11] S. Silber, H. Grabner, R. Lohninger, and W. Amrhein, "Design aspects of bearingless torque motors," in *Proceedings of the 13th International Symposium on Magnetic Bearings*, 2012.

[12] S. Silber, W. Koppelstätter, G. Weidenholzer, G. Segon, and G. Bramerdorfer, "Reducing development time of electric machines with symspace," in *Proceedings of the 8th International Electric Drives Production Conference*, 2018.

[13] D. Meeker, *Finite element method magnetics*, version 4.2, User's Manual, 2020.